Friction **12**(6): 1176–1193 (2024)
https://doi.org/10.1007/s40544-023-0793-z
ISSN 2223-7690
CN 10-1237/TH
RESEARCH ARTICLE

A new 3D plastoelastohydrodynamic lubrication model for rough surfaces

Shengyu YOU, Jinyuan TANG*, Qiang WANG
State Key Laboratory of Precision Manufacturing for Extreme Service Performance, Central South University, Changsha 410083, China
Received: 30 March 2023 / Revised: 04 June 2023 / Accepted: 01 July 2023

Abstract: Plastoelastohydrodynamic lubrication of rough surfaces (R-PEHL) is a cutting-edge area of research in interface fluid-structure coupling analysis. The existing R-PEHL model calculates the elastic-plastic deformation of rough surface by the Love equation in a semi-infinite space smooth surface, which deviates from the actual surface. Therefore, it is an innovative work to study the exact solution of elastic-plastic deformation of rough surface and its influence on the solution results of R-PEHL model. In this paper, a new contact calculation model of plastoelastohydrodynamic lubrication (PEHL) with three-dimensional (3D) rough surface is proposed by integrating numerical method of EHL and finite element method. The new model eliminates an original error introduced by the assumption of semi-infinite space in contact calculation, providing wide applicability and high accuracy. Under the given rough surfaces and working conditions, the study reveals that: (1) the oil film pressure calculated by the new model is lower than that of the smooth surface in semi-infinite space by 200–800 MPa; (2) the Mises stress of the new model is 2.5%–26.6% higher than that of the smooth surface in semi-infinite space; (3) compared with the semi-infinite space assumption, the rough surface plastic deformation of the new model is increased by 71%–173%, and the local plastic deformation singularity may appear under the semi-infinite space assumption; (4) the plastic deformation caused by the first contact cycle on the rough surface of the new model accounts for 66.7%–92.9% of the total plastic deformation, and the plastic deformation of the semi-infinite space accounts for 50%–83.3%. This study resolves the contradiction between the smooth surface assumption and the rough surface in the existing R-PEHL model, establishing a solid logic foundation for the accurate solution of R-PEHL model.

Keywords: rough surface; plastoelastohydrodynamic lubrication (PEHL); asperity plastic deformation; semi-infinite space

1 Introduction

Gears, bearings, and other machine parts involve surface friction during operation, which result in energy loss and surface wear. Therefore, lubrication is essential for preventing wear and reducing friction, and good lubrication condition is an important guarantee for the normal service of equipment. In 1886, Reynolds [1] proposed the hydrodynamic lubrication theory for the first time. On this basis, Dowson and Higginson [2] introduced the inverse solution method to successfully solve the problem of slow convergence of direct iterative algorithm of hydrodynamic lubrication equation, and gave a complete numerical solution of the line contact elastic hydrodynamic lubrication (EHL) problem. The numerical solution couplings the hydrodynamic lubrication equation with the elastic deformation equation of solid. Later, on the basis of Dowson's EHL theory, researchers expanded on this work in many directions, such as point contact EHL, thermal EHL, rough surface mixed EHL, non-Newtonian fluid EHL,

* Corresponding author: Jinyuan TANG, E-mail: jytangcsu@163.com

Nomenclature

a	Hertz contact half width (μm)	u_{max}	Maximum deformation (μm)
E	Elasticity modulus (MPa)	v	Poisson ratio
F	Linear load (N/mm)	v^e	Eelastic deformation of solid surface (μm)
h	Thickness of oil film (μm)	v^p	Plastic deformation of solid surface (μm)
h_0	Geometric interval of contact surface topography (μm)	x, y, z	Space coordinates (μm)
		α	Pressure–viscosity coefficient (Pa^{-1})
n	Hardening exponent	ε_p	Plastic strain
p	Contact oil film pressure (MPa)	η	Viscosity of lubricating oil (Pa·s)
p_H	Maximum Hertz contact pressure (MPa)	η_0	Ambient viscosity of lubricating oil (Pa·s)
p_{max}	Maximum contact pressure (MPa)	ρ	Density of lubricating oil (kg/m^3)
R	Equivalent radius of contact cylinder surface (μm)	ρ_0	Ambient density of lubricating oil (kg/m^3)
		σ	Yield stress (MPa)
R_d	Surface deformation relative error	σ_Y	Initial yield strength (MPa)
t	time (s)	σ_{max}	Maximum Mises stress (MPa)
u	Surface plastic deformation (μm)	τ_0	Characteristic shear stress (MPa)
u_r	Entrainment velocity (m/s)		

and plastoelastohydrodynamic lubrication (PEHL). Ranger et al. [3] studied the numerical algorithm of elastohydrodynamic lubrication for ellipsoidal contact based on Dowson's method, and presented the classic oil film thickness distribution image of point contact. The increase in temperature caused by fluid lubrication leads to the decrease of lubricating oil viscosity, resulting in the decrease of oil film thickness, which worsens the surface lubrication conditions. Consequently, the lubrication heat effect in EHL has gradually attracted the attention of researchers. For example, Cheng [4] introduced the thermal effect into EHL, solved the governing equation of EHL coupled with the energy equation, and obtained the temperature variation between contact surfaces. Zhu and Wen [5] developed a complete numerical solution of point-contact thermal-elastohydrodynamic lubrication (TEHL), and found that the oil film temperature increases significantly in the contact area and changes little in the inlet area due to entrainment. Hsu and Lee [6] studied the influence of dimensionless load, slide–roll ratio, and thermal effect on the oil film thickness of slide–roll contact in TEHL. Ghosh and Pandey [7] examined the thermal-elastohydrodynamic problem under the contact condition of heavy-duty lines and found that the thickness of oil film decreased significantly compared with that under isothermal condition.

The real surface at the micron scale contains numerous asperities, and it is ideal that the asperities are fully separated by oil film between contact surfaces. During the contact loading process, locally high asperities puncture the oil film, leaving only nanometer-thick film between the surface asperities, resulting in "dry contact" [8]. According to the area of dry contact, rough surface EHL can be classified into boundary lubrication, mixed lubrication, and full film lubrication [9]. Solid contact in mixed lubrication brings challenges to solve the overall Reynolds equation. Xu and Sadeghi [10] analyzed the impact of surface roughness on contact properties under thermoelastohydrodynamic conditions by employing the measured roughness surface and solving the two-dimensional Reynolds and energy equations. Hu and Zhu [5, 11] suggested a numerical solution for the point-contact mixed lubrication, which partitioned the contact area into separate lubrication and dry contact models based on the contact state. They solved these two models independently and then integrated them into the Reynolds equation framework. The dynamic pressure term in the equation vanishes during dry contact, yielding a unified pressure equation. This

approach can accommodate most lubrication states and satisfy a wide range of working conditions, thereby laying the groundwork for the development of EHL numerical solution methods for deterministic rough surfaces. Ren et al. [12] performed three-dimensional (3D) line contact mixed lubrication modeling using Hu's EHL model and analyzed the effect of differing roughness on lubrication performance. Zhu et al. [13] focused on the influence of varying numerical solution techniques on the accuracy of the mixed lubrication model, and found that making the surface mesh density greater than that of the solution domain can decrease the error.

The presence of surface asperities causes local surface contact pressure to be several times higher than the maximum Hertz contact pressure, resulting in extreme stress concentrations near the asperities. Many studies have indicated that the surface material of rough surfaces already experience elastoplastic contact at low load levels. In the study of elastoplastic contact numerical method, Jacq's elastoplastic contact method (SAC) [14] provides a 3D elastoplastic contact stress calculation framework which integrates four methods, namely elastic contact numerical method [15], contact stress numerical method [16], residual stress and residual deformation calculation method [17–19], and stress updating method [20]. The calculation of contact residual stress and surface plastic deformation is based on the assumption of semi-infinite space, which has certain limitations. Ren et al. [21] proposed a point-contact PEHL model by substituting the elastic contact algorithm in Jacq's elastoplastic contact method with the EHL numerical solution method. By accounting for the elastoplastic deformation and plastic yield hardening properties of materials, they obtained more accurate and reliable pressure distribution, oil film thickness, sub-surface stress, and surface topography evolution. Due to its operability and universality, Ren's PEHL numerical method has gradually become the main method in PEHL research. Building upon previous research, He et al. [22, 23] further explored the lubrication properties of PEHL with finite long line contact and point contact, revealing that the presence of plastic deformation results in a more even distribution of load across the asperity. In the rolling contact cycle, due to the plastic yield hardening of the material, the plastic strain increment gradually reaches a stable value or decrease to zero during a single contact cycle. Abdullah et al. [24] established a simplified PEHL model, in which it is presumed that the lubricating oil film pressure in the plastic deformation zone reaches a fixed limit value. However, this assumption is only valid for the case of minimal plastic strain in the elastic-perfectly plastic material. Thomas et al. [25] introduced a novel method for simulating TEHL in commercial finite element software, demonstrating its flexibility and simplicity through simulation calculations of lubrication friction coefficient, coating surface, and non-smooth surface. However, this method encounters issues when analyzing contacts on rough surfaces with vast data. Zhou et al. [26] analyzed the contact performance of surface-hardened gears by establishing a PEHL model that considers hardness gradient and surface roughness. They used Dang Van multi-axial fatigue criterion to assess the contact fatigue damage based on the contact stress field. The study evaluated the effects of effective hardening layer depth, surface hardness, and surface roughness on contact properties. Cao et al. [27] modified the surface microstructure using grinding. Based on Zaretsky's fatigue model combined with elastic contact mechanics, the rolling contact fatigue life of different rough surfaces in EHL was calculated, and the optimal topography features were determined that could mitigate the fatigue failure of micro pitting corrosion.

In conclusion, the study and application of hydrodynamic lubrication have been extensively developed. The PEHL Reynolds equation for the solid elastoplastic contact deformation calculation of rough surfaces is based on the semi-infinite space assumption with a smooth surface, which is contradictory to the rough surface PEHL analysis. Ren's model [21], based on a smooth semi-infinite space assumption, is the most widely used and efficient model in current rough surface PEHL numerical methods. Therefore, there is an urgent need to propose a new model that improves Ren's model and addresses the logical contradictions in the calculation principles of elastic-plastic contact deformation of rough surfaces. As a solution, this paper proposes a new 3D rough surface plastoelastohydrodynamic lubrication (R-PEHL)

model by coupling the numerical method of EHL with the finite element method. The numerical method of EHL allows the calculation of contact oil film pressure, and the finite element method enables accurate modeling of the rough surface topography and the precise calculation of surface asperities deformation. The new model resolves the issue of calculation accuracy of PEHL on rough surfaces resulting from the assumption of semi-infinite space smooth surface in Ren's PEHL model. Moreover, this R-PEHL model has strong applicability in the dynamic lubrication analysis of engineering components, which takes into account surface integrity.

2 Equation of R-PEHL

2.1 Hydrodynamic lubrication equation

The hydrodynamic lubrication equation is derived from the Reynolds equation, where the position of the lubrication region (x, y) satisfies the governing Eq. (1) [28]. The elastoplastic contact analysis is related to the solids of the contact surface and coupled with the thickness of the oil film.

$$\frac{\partial}{\partial x}\left(\frac{\rho h^3}{12\eta}\frac{\partial p}{\partial x}\right)+\frac{\partial}{\partial y}\left(\frac{\rho h^3}{12\eta}\frac{\partial p}{\partial y}\right)=u_r\frac{\partial(\rho h)}{\partial x}+\frac{\partial(\rho h)}{\partial t} \quad (1)$$

In Eq. (1), ρ is the density of lubricating oil, h is the thickness of oil film, η is the viscosity of lubricating oil, p is the contact oil film pressure, u_r is the entrainment velocity, and t is the time.

Affected by the bearing capacity and surface topography, the oil film thickness in some regions of the overall calculation domain of the governing equation is within the range of 2–5 nm, and the interaction between solid materials is more obvious. This contact state is referred to as "dry contact", and the corresponding governing Eq. (2) is obtained by removing the hydrodynamic pressure term in Eq. (1).

$$u_r\frac{\partial(\rho h)}{\partial x}+\frac{\partial(\rho h)}{\partial t}=0 \quad (2)$$

The oil film thickness is calculated as

$$h(t)=h_0+v^e(x,y)+v^p(x,y) \quad (3)$$

Here, v^e and v^p are elastic deformation and plastic deformation of solid surface arising from lubricating contact, respectively. h_0 is the geometric interval of contact surface topography. Elastic deformation v^e can be obtained by the integral equation of Johnson contact mechanics [29] and will not be elaborated here. Plastic deformation v^p permanently changes the surface topography, which is the focus of this study. The differences in plastic deformation calculation between the new model and the Ren model will later be compared in the paper.

The Reynolds equation described previously involves parameters with large differences in magnitude, and can lead to data errors in its solution. Therefore, the Reynolds equation is dimensionless as Eq. (4):

$$\frac{\partial}{\partial X}\left(\varphi\frac{\partial P}{\partial X}\right)+\frac{\partial}{\partial Y}\left(\varphi\frac{\partial P}{\partial Y}\right)=\frac{\partial\left(\bar{\rho}H\right)}{\partial X}+\frac{\partial\left(\bar{\rho}H\right)}{\partial T} \quad (4)$$

Here, $X = x/a$, $Y = y/a$, $P = p/p_H$, $H = hR/a^2$, $\bar{\rho} = \rho/\rho_0$, $\varphi = p_H\rho h^3R/12\eta u_r a^3$, a is the Hertz contact half width, p_H is the maximum Hertz contact pressure, and R is the equivalent radius of contact cylinder surface.

Similarly, the dry contact region in the Reynolds equation of dimensionless form is as Eq. (5):

$$\frac{\partial\left(\bar{\rho}H\right)}{\partial X}+\frac{\partial\left(\bar{\rho}H\right)}{\partial T}=0 \quad (5)$$

Based on the numerical solution method proposed by Zhu [5] and the lubricating oil characteristic equation consistent with the references, the finite difference method is used to discreetly solve the Reynolds equation, and the Gauss Seidel method is adopted to iterative calculation. The dimensionless oil film pressure P converges iteratively after satisfying Eq. (6):

$$\frac{\sum\sum\left|P_{i,j}-P_{i,j}^{\text{old}}\right|}{\sum\sum P_{i,j}^{\text{old}}}\le 10^{-3} \quad (6)$$

2.2 Calculation process and plastic deformation v^p calculation in the Ren model

Under lubrication condition, the contact pressure between the two contact surfaces is transmitted via

the lubricating oil film. In the case of pure elastic contact, surface deformation recovers after unloading, and the contact stress under the surface can be evaluated based on the elastic contact pressure. In elastoplastic contact, the asperity at the micron scale is easy to undergo plastic deformation, thereby permanently modifying the topography of the contact surface and affecting the lubricating oil film and contact pressure distribution. Therefore, in order to solve the contact properties of plastoelastohydrodynamic lubrication, it is necessary to consider the coupling of contact stress, contact pressure, plastic deformation, and fluid lubrication. Ren proposed a PEHL model of point-contact, and the calculation process is depicted in Fig. 1(a). The specific calculation steps are as follows: (1) calculate the oil film pressure P of a rough surface using the EHL numerical method, assuming pure elastic deformation; (2) simplify the rough surface to a smooth surface, and assume that the calculation region Ω is a semi-infinite space. Here, the contact stress field in the discretized region Ω is calculated according to EHL pressure P; (3) superimpose the elastic contact stress field onto the potential residual stress field of plastic deformation. Then, compute the elastoplastic contact stress field and plastic strain corresponding to the comprehensive stress field in the region Ω by applying the material constitutive model and the stress updating numerical algorithm; (4) calculate the plastic residual stress and surface cumulative residual deformation in the calculation region Ω from the plastic strain. The residual deformation is the solid surface plastic deformation v^p in Eq. (3), while the surface cumulative residual deformation is computed via Love equation [16]; (5) repeat the steps (1)–(4) for updating rough surface topography based on the surface plastic deformation v^p, and realize the calculation cycle iteration until the convergence conditions are met.

Considering that the stiffness of the material after plastic yield decreases and the corresponding deformation increases, the plastic deformation v^p at the elastoplastic deformation stage of the asperity of the contact surface is difficult to ignore compared with the elastic deformation. While the Ren's PEHL

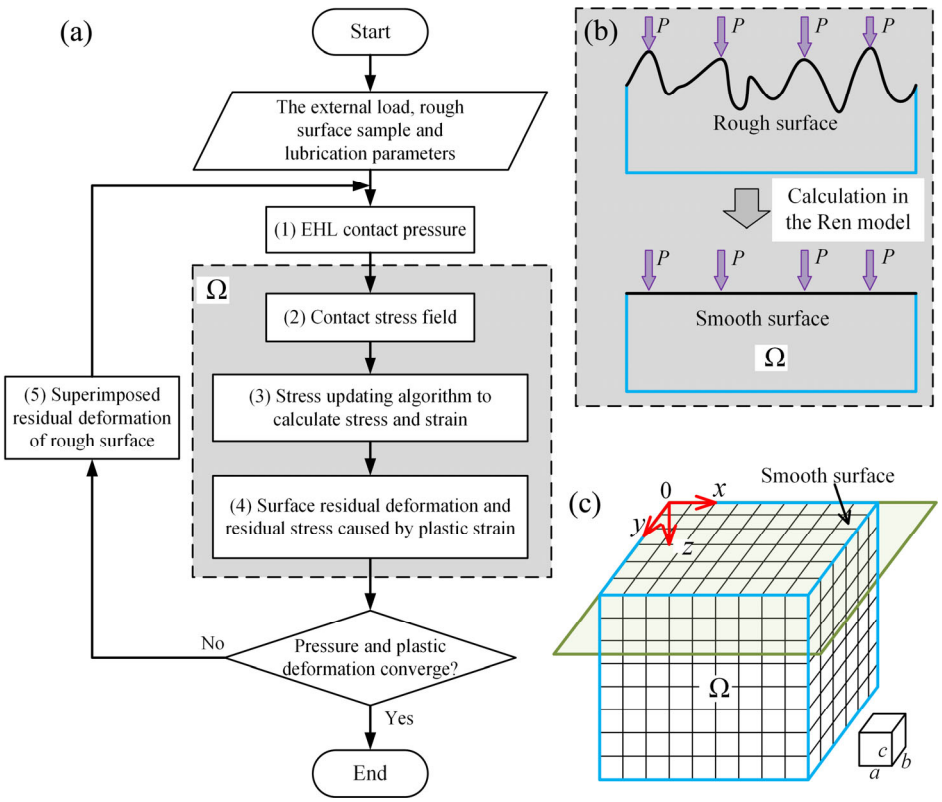

Fig. 1 Flow chart and calculation region of the Ren model. (a) Flow chart; (b) surface topography simplification; and (c) discrete computing region.

model based on this method has been widely used, it suffers from a primitive error in the plastic deformation v^p of the rough surface. Figure 1(b) illustrates the calculation process of the contact stress field in step (2). In step (2), the EHL pressure P is calculated from the 3D rough surface topography. Because it is difficult to obtain a numerical solution for contact stress and strain under a rough surface, the contact stress field beneath the surface is derived by applying the EHL pressure P to the discrete calculation region Ω with a smooth surface. Here, the rough surface is reduced to a smooth surface of region Ω in step (2), and the region Ω is discretized in numerical calculation as depicted in Fig. 1(c). This region Ω conforms to the assumption of semi-infinite space, and the numerical calculations of subsequent step (3) and step (4) are performed in the region Ω. In step (4), the plastic deformation of smooth surface calculated in the region Ω is taken as the plastic deformation of rough surface, which creates an evident contradiction. The disparity between the plastic deformation of rough surface and that of smooth surface is the source of the original error of PEHL analysis of rough surface in the Ren model.

2.3 Calculation process and plastic deformation v^p calculation in the new model

To circumvent the above calculation errors shown in Fig. 1(b), a finite element model was employed based on the rough surface topography. In the new model, the calculation region Ω from step (2) to step (4) in Ren's model is replaced with a finite computation region that consists of finite elements, and the contact plastic deformation v^p corresponds to each surface asperity. The EHL pressure of rough surface was applied to the finite element model with the same topography, as illustrated in Fig. 2. The method of modeling the rough surface finite element mesh model was referred to Refs. [30, 31]. The rough surface topography was mapped to the surface of the finite element model by adjusting the coordinate values of mesh nodes, this method preserves all topography features of the rough surface sample, and the surface roughness parameters of the finite element model are consistent with the sample. The

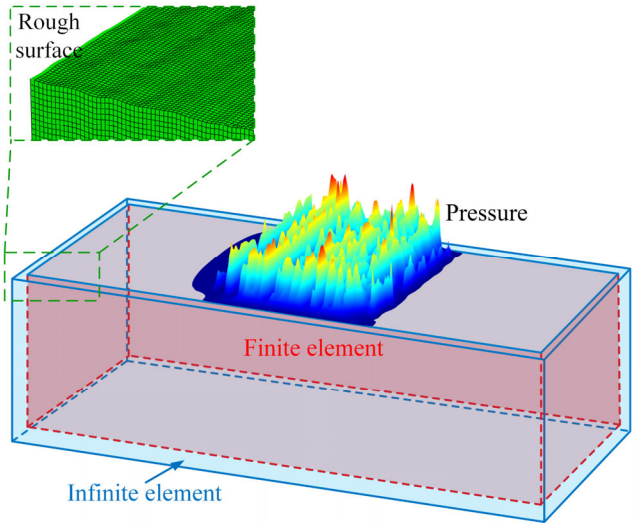

Fig. 2 Finite element model of contact stress calculation.

presence of finite boundaries in the finite element model may cause contact stress-strain to be affected by boundary conditions. During the loading process, contact stress waves are reflected from the boundary of the finite element model into the model, and resulting in an imprecise contact stress field. Thus, the boundary finite elements of the model are replaced with infinite elements in this method. As depicted in Fig. 2, the rough surface bearing loading pressure in the model is finite element, while the outermost elements of the other five surfaces are infinite elements. This technique partially mitigates the influence of the model boundary on the calculation results.

The calculation process of the new and improved plastoelastohydrodynamic lubrication contact model is depicted in Fig. 3. The plastic deformation of asperities is more in line with the actual rough surface deformation, and the EHL contact analysis has been performed based on existing numerical method. Finite element modeling and plastic deformation calculations were executed through the static implicit solver of commercial finite element software ABAQUS, utilizing hexahedral linear reduced integration element C3D8R for finite element type and hexahedral element CIN3D8 for infinite element type. Regarding the material constitutive, an isotropic assumption commonly used in the deformation of metallic materials was adopted. The plastic deformation stage satisfies the J_2 plastic flow theory, and the radial

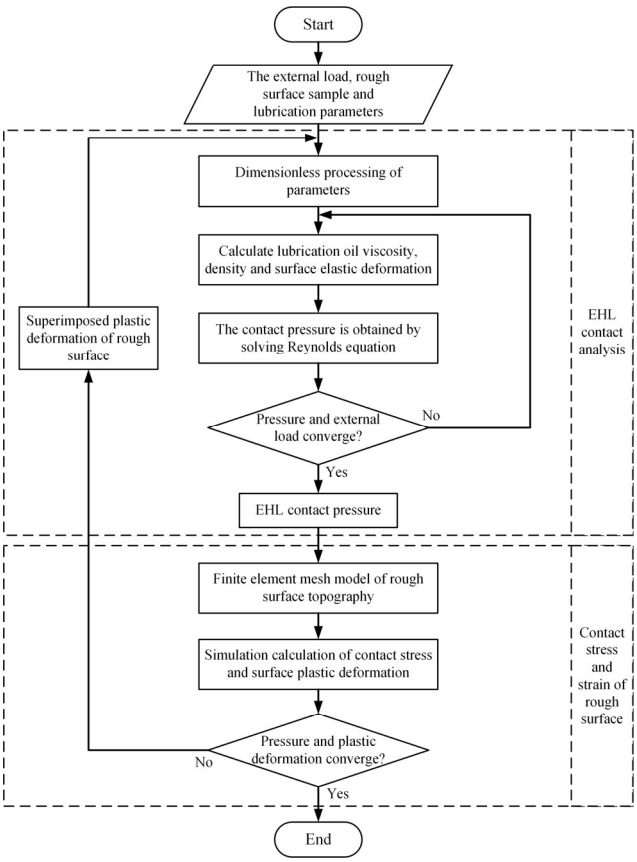

Fig. 3 Calculation flowchart of the new model.

return algorithm was employed in finite element analysis for stress updates [32]. The convergence of the model's calculation flow is determined by Eqs. (6) and (7). Several examples indicate that convergence of contact pressure P is considerably quicker than the convergence of surface plastic deformation v^p, it means that the convergence of the calculation flow can be judged only by Eq. (7). EHL can yield oil film pressure without an upper limit, and this may lead to exceptionally high elastic contact pressure on the finite element mesh, resulting in the mesh distortion which makes the calculation difficult to converge. The new model limits the oil film pressure obtained by EHL to a threshold value of 2.83 times the maximum yield strength of solid materials, following plastic strain hardening. The truncated oil film pressure renders the actual total external load less than the required total external load, and hence the new model employs it to achieve the convergence of the PEHL calculation. Then, it proceeds with increased loading for PEHL contact analysis, enabling the total load to meet the calculation requirements. Experimental verification through contact stress and strain measurement becomes challenging because of the small size of the rough surface asperity [33], which is also a difficulty in the present analysis of rough surface PEHL contact. Zhang et al. [34] measured the elastoplastic contact pressure of the surface under extreme roughness, and the finite element calculation data produced favorable agreement with the measured results. For the reason that commercial finite element software has been widely utilized for contact analysis and the paper's model of finite element and material constitutive are not fundamentally different from those in this literature. Therefore, to some extent, the accuracy of the finite element plastic deformation calculation in this paper can be indirectly proved.

$$\frac{\sum\sum\left|v_{i,j}^{p}-\left(v_{i,j}^{p}\right)^{\text{old}}\right|}{\sum\sum\left(v_{i,j}^{p}\right)^{\text{old}}}\le 10^{-3} \tag{7}$$

3 Calculation example

The study employs the new model and the Ren model to analyze PEHL of rough surface. The three surface topographies used are shown in Fig. 4. All the three surfaces are processed by Gaussian filtering. The sampling interval is 5 μm × 5 μm, and the roughness Sq values for samples S1, S2, and S3 are 0.47, 0.42, and 0.41 μm, respectively. The measured rough surface topographies have fixed texture directions, S1 is the grinding surface and S2 is the working surface of gear. Sample S3 is a reconstructed surface generated by fast Fourier transform [35], with asperities height that comply with the Gaussian random distribution. The 2D topographies correspond to the intercepted topography at the position of the red line of the three samples, and S2 is the gentlest surface due to gear contact run-in. Lubrication parameters are listed in Table 1. In the EHL contact analysis of Fig. 3, the study employs a rough surface whose lubricating contact with a rigid surface rough is displayed in Fig. 5, a line load F along the y axis is applied on the rigid surface, and the surface rolls and slips along the x axis direction. The boundary of the calculation area of the rough surface is prone to

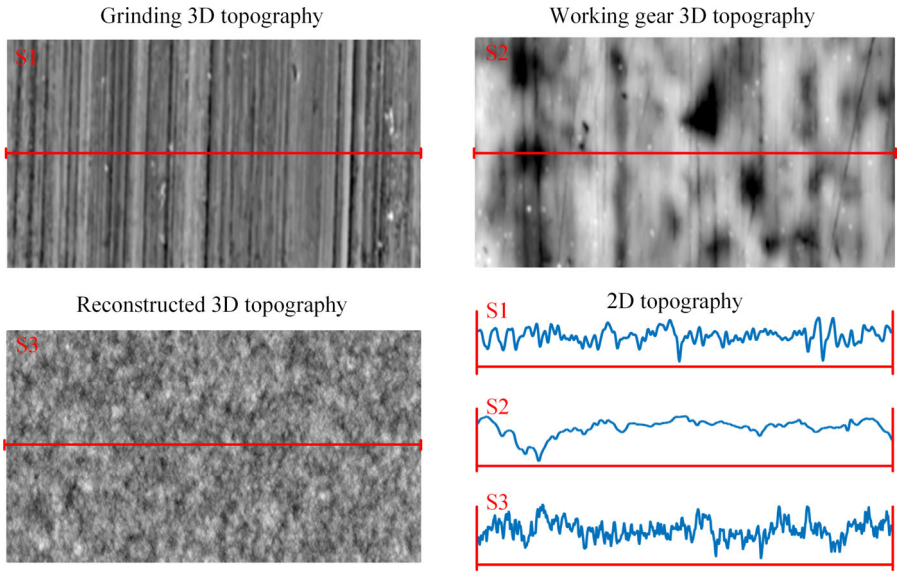

Fig. 4 Topographies of three types of samples.

Table 1 PEHL calculation parameters.

Parameter	Value	Parameter	Value
Linear load F (N/mm)	710	Ambient density of lubricating oil ρ_0 (kg/m^3)	870
Elasticity modulus E (MPa)	210,000	Ambient viscosity of lubricating oil η_0 (Pa·s)	0.05
Poisson ratio v	0.3	Pressure-viscosity coefficient α (Pa^{-1})	2.1×10^{-8}
Hertz contact half width a (μm)	300	Characteristic shear stress τ_0 (MPa)	5
Hertz maximum pressure p_H (MPa)	1,506	Initial yield strength σ_Y (MPa)	1,000
Entrainment velocity u_r (m/s)	1.56	Hardening exponent n	0.2

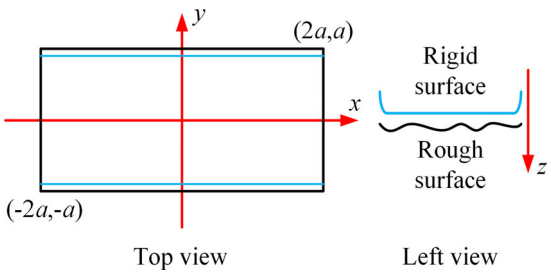

Fig. 5 Schematic diagram of EHL contact analysis.

abnormally high contact stress, so the two ends of the rigid cylindrical surface are warped upward to avoid edge contact. In the stress and strain calculation of Fig. 3, the contact surface size of the finite element mesh model is consistent with Fig. 5 and the model thickness along the z axis is 1.5a, where the finite element mesh size is 5 μm × 5 μm and thickness of 10 μm. The total mesh number of the model is 1,296,000, and the calculated surface is the local part of the three samples in Fig. 4. Plastic deformation hardening for contact surface material is considered, and the power rate hardening model of Eq. (8) is adopted to describe the relationship between yield stress σ and plastic strain ε_p after plastic yield. Table 1 lists the values of parameters in the power rate hardening equation.

$$\sigma=\sigma_Y\left(1+\frac{E}{\sigma_Y}\varepsilon_p\right)^n \tag{8}$$

4 Results and discussion

4.1 Lubrication film pressure and contact stress

The PEHL analysis between smooth surface and rough surface was carried out based on the proposed new model, and the contact oil film pressure is shown in Fig. 6. Figure 6(a) shows a surged of edge contact pressure due to the warping of the contact edge in

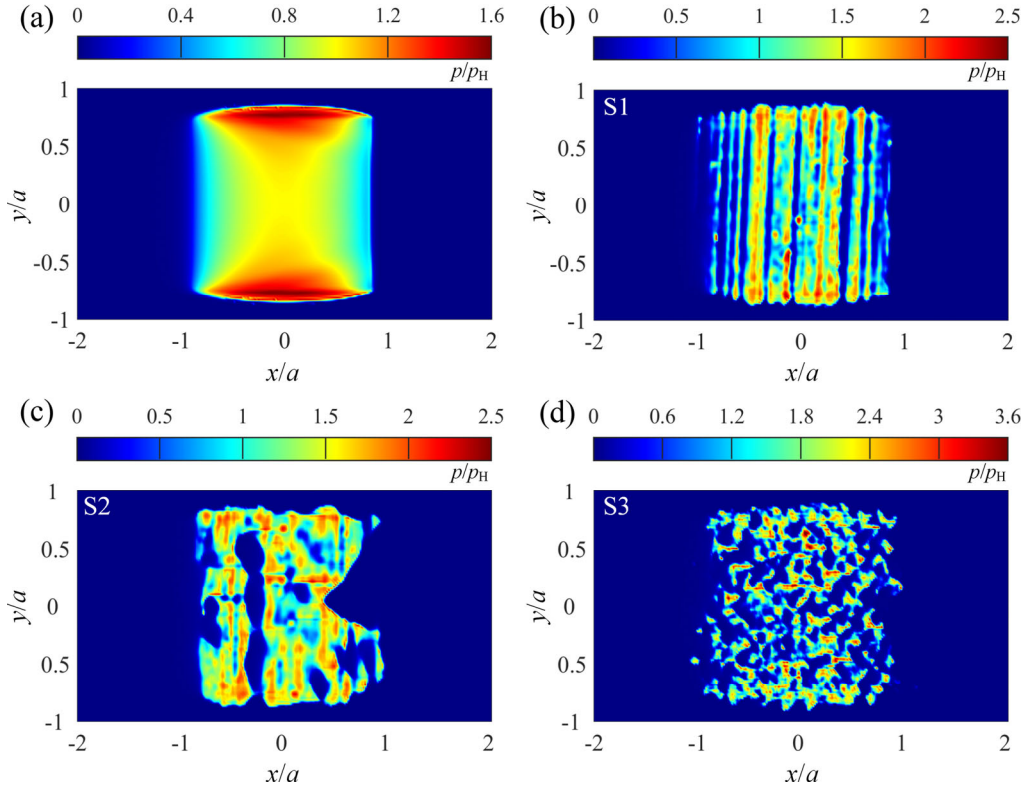

Fig. 6 Lubrication contact pressure. (a) Smooth surface; (b) S1; (c) S2; and (d) S3.

two sections, resulting in a maximum contact oil film pressure. This is different from the assumption that the oil film pressure distribution remains unchanged in the normal motion direction of line contact. Figures 6(b)–6(d) also show that the maximum contact pressure for the elastoplastic contact pressure of rough surface appears in the edge of contact area, and the overall pressure distribution is similar to the topography characteristics of corresponding rough surface samples in Fig. 4. The lubricating oil film affects the change of extreme pressure of the contact surface to some extent. The lubrication contact pressure obtained from the reconstructed samples is very discrete, indicating that the lubrication contact analysis of such surfaces deviates from the engineering practice.

To compare the new R-PEHL model with the Ren model, the height sequence data for each rough surface sample were multiplied by different multiples, resulting in three samples with varying roughness *S*q. Figures 7, 8, and 9 show the calculated distribution of sectional contact pressure and film thickness at the same location on each surface. At the minimum *S*q, the contact surface of each sample topography is entirely separated by the lubricating oil film, which is in the optimal state of full-film lubrication. The contact surface's asperities have a minimal effect on the distribution of the lubricating oil film, and while the overall level of contact pressure increases, the distribution characteristics similar to those of smooth surface lubricating oil film pressure can still be seen. As the roughness *S*q increases, higher asperities on the surface make direct contact with the solid surface through the lubricating oil film, causing a sharp increase in surface contact pressure due to the plastic yield strengthening of the asperity material. By analyzing the surface pressure of different samples with the maximum roughness *S*q = 0.72 μm, *S*q = 0.68 μm, and *S*q = 0.63 μm, it can be seen that the maximum contact pressure of local oil-film-free lubrication increases significantly with an increase in roughness, which indicates that the maximum contact pressure under mixed lubrication depends mainly on the degree of contact deformation of asperities. The contact oil film pressure differs due to the varied calculation methods of contact plastic deformation

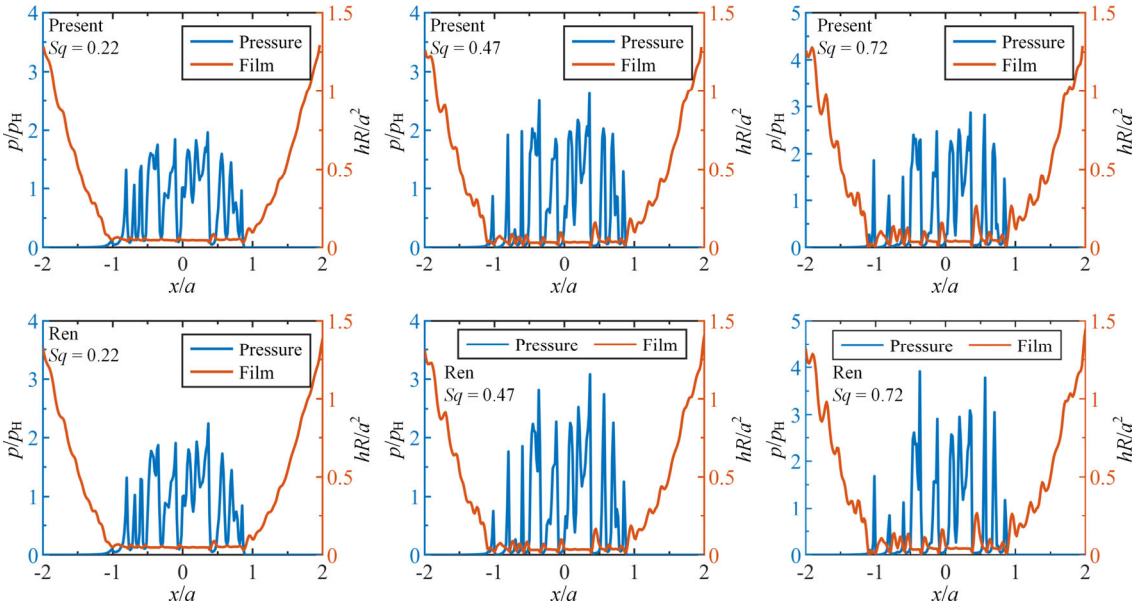

Fig. 7 Comparison of pressure and oil film thickness under different roughness (Sample S1).

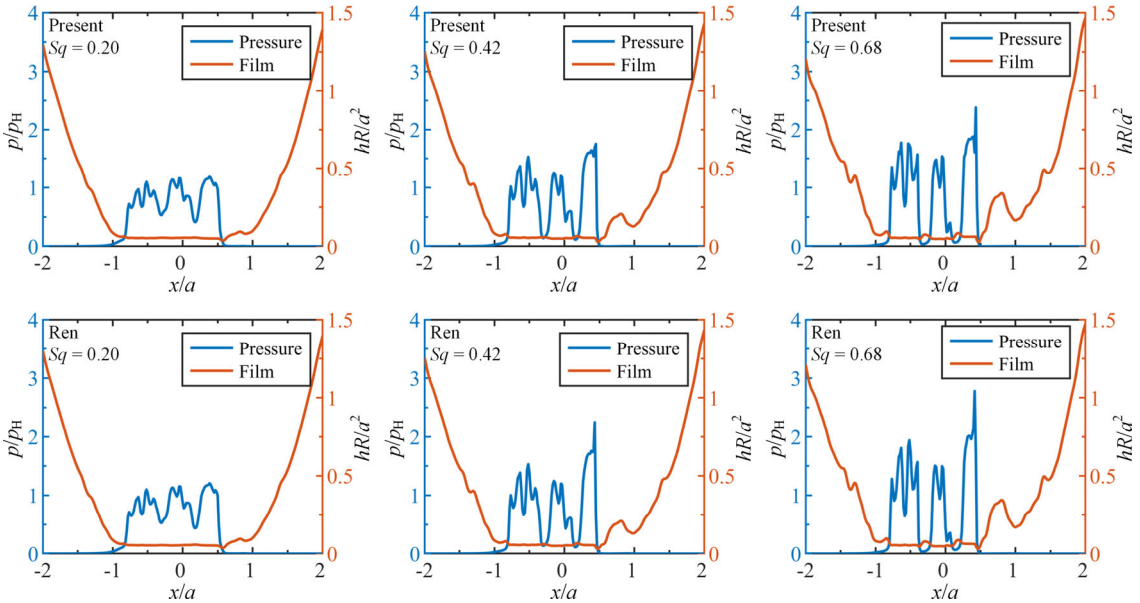

Fig. 8 Comparison of pressure and oil film thickness under different roughness (Sample S2).

between the present model and the Ren model [15]. As observed in Figs. 7, 8, and 9, the overall contact pressure amplitude of the present model under different roughness is smaller than that of the Ren model, and the contact pressure in the present model changes more gradually. This phenomenon is most noticeable in sample S3 (Fig. 9) with more asperities and generates greater plastic strain. When the surface is rougher, the higher contact pressure in the Ren model is biased to the direction of the oil outlet on the right side of the Fig. 9, whereas the contact pressure distribution calculated by the present model does not deviate significantly.

After the contact calculation of PEHL satisfied the convergence condition shown in Fig. 3, the contact stress component under the elastoplastic contact surface was obtained using Python secondary development techniques. The x–z cross-section Von Mises stress of sample S1 is shown in Fig. 10. The contact stress on a smooth surface is approximately consistent with the

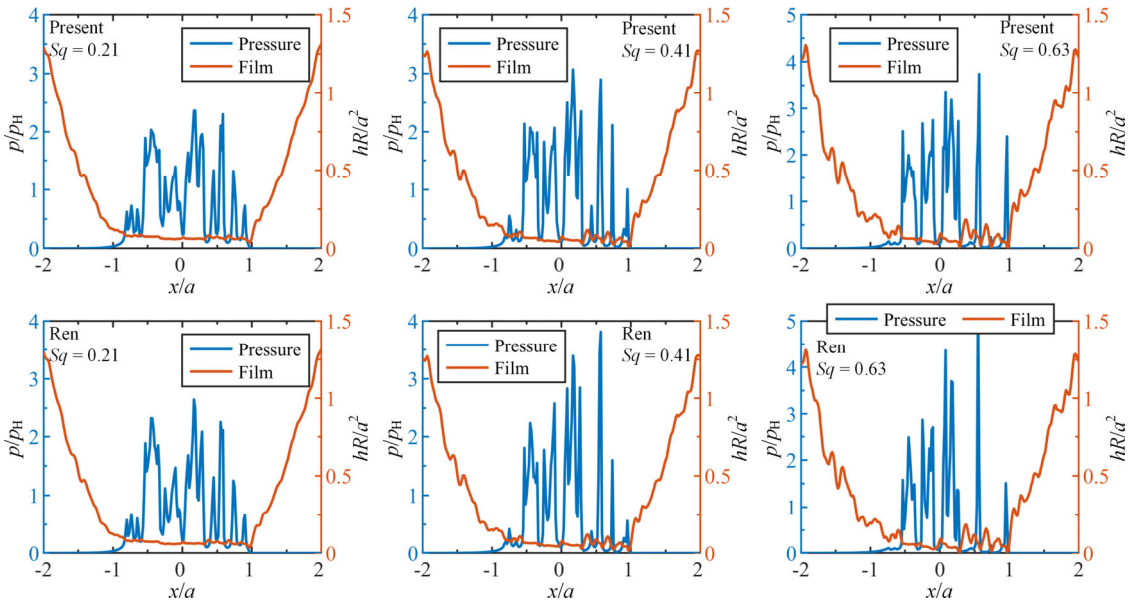

Fig. 9 Comparison of pressure and oil film thickness under different roughness (Sample S3).

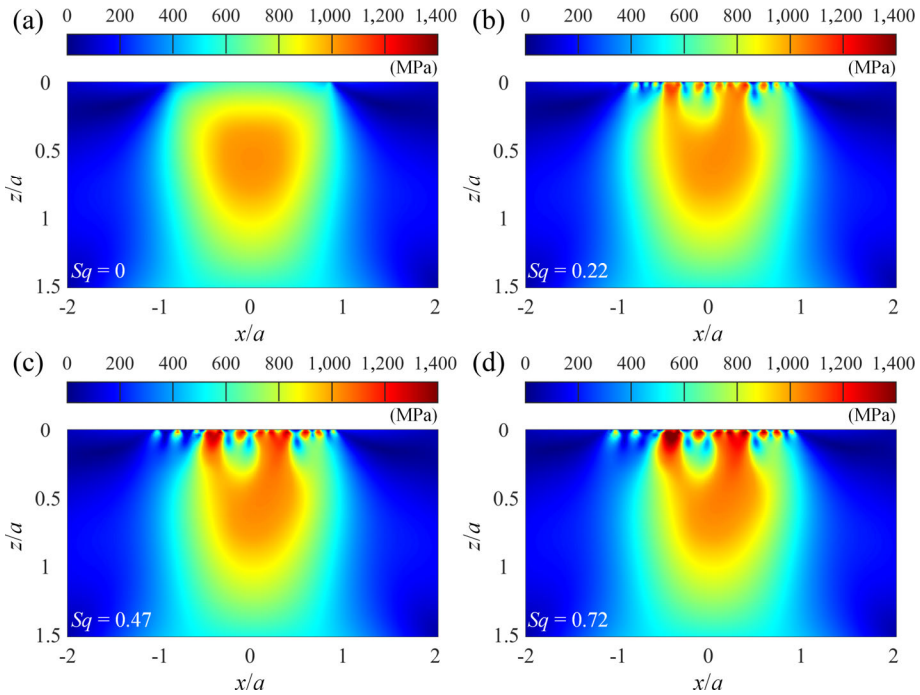

Fig. 10 Comparison of Von Mises stress on sub-surface with different roughness (Sample S1). (a) *S*q = 0; (b) *S*q = 0.22 μm; (c) *S*q = 0.47 μm; (d) *S*q = 0.72 μm.

Hertzian contact stress field, and a small peak in contact stress appears at the secondary peak of contact pressure under oil film lubrication. At *S*q = 0.22 μm, two regions with higher stress are observed, one near the surface and another at greater depth. The contact stress of rough surface asperities with greater plastic deformation is higher than that at greater depth. The impact depth of contact stress in the area near the surface increases with increased *S*q, and the high-stress region in the deeper area fuses with the near-surface stress field. The maximum contact stress occurs near the asperity with high plastic surface deformation. This trend is also observed in dry contact, but the corresponding roughness *S*q is smaller. It can

be seen that the lubricating oil film enlarges the surface contact area, thus alleviating the stress concentration near the asperity of the contact surface.

Table 2 shows the maximum contact pressure p_{max} and maximum subsurface Von Mises stress σ_{max} on different rough surfaces. The maximum surface contact pressure in the present model is approximately 200–800 MPa lower than in the Ren model, and the bearing capacity of asperities depends on the yield strengthening strength of materials. The maximum contact pressure pmax in the present model is about 6 GPa under the roughness *S*q = 0.63 μm of sample S3. In contrast, the maximum contact Mises stress is higher under rough surfaces in the present model than in the Ren model, ranging from 2.5% to 26.6% in Von Mises stress. Surface pressure directly acts on the corresponding asperity in the present model, making contact deformation more likely to occur than on a smooth surface. Consequently, the subsurface contact stress obtained is significantly higher than in the Ren model. The semi-infinite space assumption in the Ren model overestimates surface contact pressure and underestimates subsurface contact stress, and the deviation value decreases with the increase of plastic deformation degree.

4.2 Plastic deformation of contact surface

4.2.1 Surface plastic deformation

The distribution of asperity heights on the lubrication contact rough surface is random, resulting in discrete surface plastic deformation. Calculation of surface deformation in the present model is different from that in the Ren model. Taking sample S1 as an example, the comparison of deformation region between the two models is shown in Fig. 11. Figures 11(a) and 11(b) show the plastic deformation diagrams of the contact surface for the present model and the Ren model, respectively. To facilitate a visual comparison of the deformation distribution, the paper depicts the contact area with deformation greater than 0.1 μm as a dark area. Clearly, the deformation area of the present model is larger. This is because the semi-infinite space assumption in the Ren model makes the contact stress gentler, and it is difficult to capture the deformation of lower local asperities. Figures 11(c) and 11(d) compare the sectional deformation between the edge and center of the contact region for both models. Greater contact pressure at the edge leads to more deformation of the corresponding contact surface. In general, the surface deformation of the present model is higher than that of the Ren model, especially in cases with high local asperities where there exists a noticeable difference in deformation. When the solid on the contact surface is squeezed, the material at the edge of deformation is protruded. Since the deformation of the Ren model is smaller than that of the present model, the protrusion degree of material at the edge of plastic deformation area is smaller than the present model.

To further investigate the surface plastic deformation characteristics of the two models, Fig. 12 shows the error distribution in the absolute value of deformation between the present model and the Ren model for different samples and different roughness. The blue area in Fig. 12 indicates higher surface plastic deformation for the present model than the Ren model, while the yellow area signifies lower surface plastic deformation. The present model has higher surface contact deformation with low roughness *S*q. With the increase of roughness, the surface deformation of the Ren model near the higher asperities becomes larger, especially the high roughness surfaces corresponding to samples S1 and S2 in Fig. 12. Due to the assumption of smooth surface in the Ren model, local contact stresses may interact with each other to cause abnormal surface deformation, as illustrated in Fig. 12 for region A of *S*q = 0.72 μm surface. Combined with Fig. 11, it can be seen that the plastic

Table 2 Maximum contact pressure p_{max} and maximum Mises stress σ_{max}.

*S*q (μm)	p_{max} (MPa)		σ_{max} (MPa)	
	Present	Ren	Present	Ren
0.22	3,337	4,045	1,282	1,013
0.47	4,960	5,801	1,458	1,339
0.72	5,899	6,119	1,895	1,624
0.20	2,758	3,130	1,288	1,186
0.42	3,728	4,026	1,327	1,231
0.68	3,951	4,343	1,377	1,309
0.21	5,300	5,546	1,453	1,417
0.41	5,841	6,084	1,810	1,632
0.63	6,010	6,293	2,006	1,744

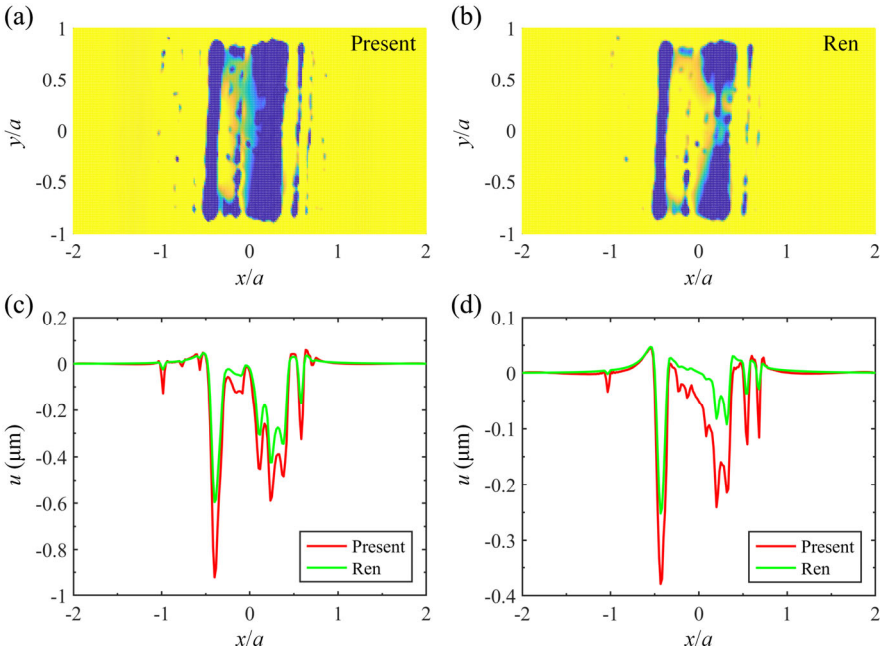

Fig. 11 Deformation comparison of rough surface with roughness *S*q = 0.72 μm. (a) Present model surface deformation; (b) Ren model surface deformation; (c) deformation comparison at y/a = -0.75; and (d) deformation comparison at y/a = 0.

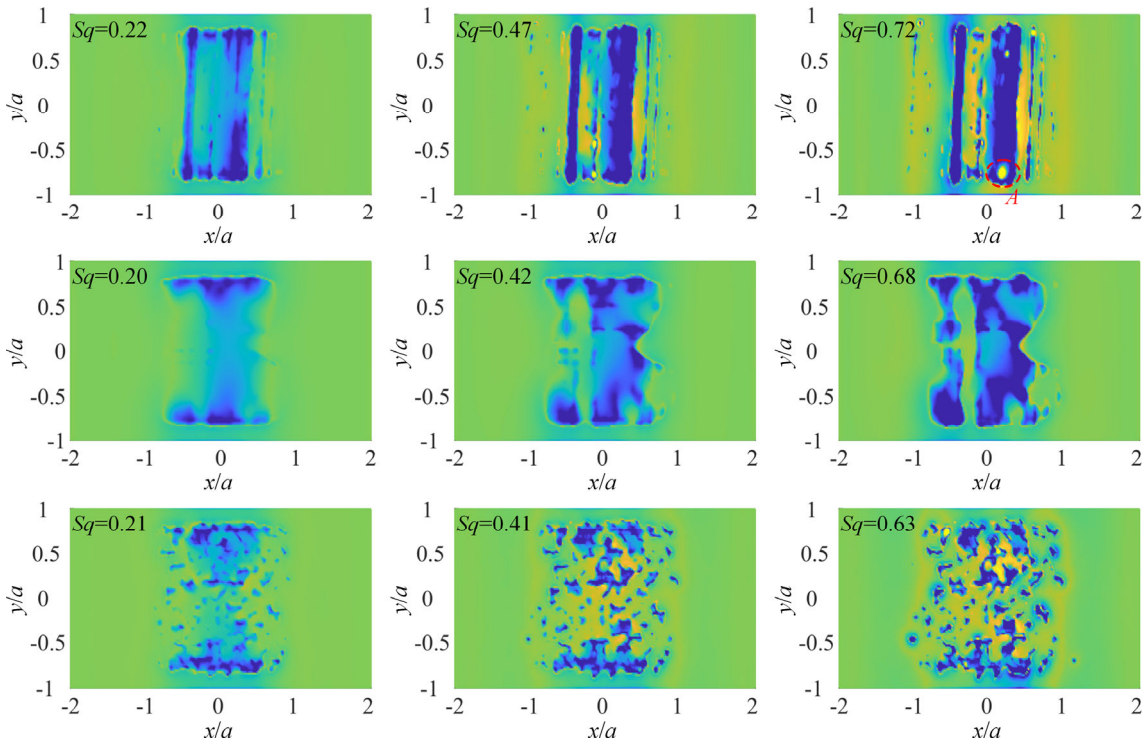

Fig. 12 Surface deformation differences under different *S*q, and each row from top to bottom corresponds to sample S1, S2, and S3, respectively.

deformation of the Ren model with large region of surface deformation appears an abnormal surge here, and a singularity with deformation greater than that of the present model appears. To further study this phenomenon, the paper calculated the relative error R_d of the total surface deformation of the present model and the Ren model, and the maximum deformation u_{max} of the present model are also

calculated, as tabulated in Table 3. The relative error of the contact deformation between the present model and the Ren model ranges from 71% to 173%, and the error is negatively correlated with *S*q. Sample S2 has the smallest surface deformation but the largest relative deformation error. In contrast, sample S1 has the smallest relative deformation error, but the surface deformation is between the other two. Thus, it should be noted that the maximum surface deformation is not necessarily tied to the overall deformation relative error. By analyzing the surface deformation distribution characteristics of different sample topographies, it can be inferred that the deformation singularity of the Ren model appears in the position with higher deformation amount and larger deformation range.

4.2.2 *Surface topography evolution*

Under the current load, the topography changes of the contact surface are dominated by the plastic deformation of the asperity in the contact area, and the unloading of the rough surface after contact loading in the lubrication is regarded as a contact cycle. The surface deformation of the rough surface for multiple contact cycles in the mixed lubrication state of the new model can be found in Figs. 13 and 14. The contact plastic deformation is mainly located in the lubrication contact center area. Unlike dry contact, the maximum deformation position in Fig. 13 after the first contact cycle does not correspond to the highest asperity, and the contact deformation of different asperities does not show a positive correlation with their heights. The deformation of the asperity is affected by the oil film pressure distribution near the contact asperity. During the contact process, the asperity flattens due to contact pressure, while the bottom material experiences a slight uplift. The deformation trend of the rough surface is gradually flat when only the contact plastic deformation is considered. Figure 14 shows the surface deformation after multiple cyclic contacts. Compared with the surface deformation of the first contact in Fig. 13, the accumulated surface deformation after multiple contact cycles is almost negligible. Surface deformation of PEHL of the rough surface under cyclic loading is still dominated by the surface deformation of the first contact, which is further supported by heavy-duty contact analysis. Considering the calculation accuracy, it is appropriate to consider that the rough surface enters a contact stable state after 5 contact cycles without the plastic deformation accumulation of the asperities, thereby allowing for contact fatigue and wear analysis based on the stress-strain field in this state.

Table 3 Surface deformation relative error R_d and maximum deformation u_{max}.

	*S*q (μm)	R_d	u_{max} (μm)
S1	0.22	1.26	0.48
	0.47	0.78	0.95
	0.72	0.71	2.19
S2	0.20	1.73	0.28
	0.42	1.67	0.33
	0.68	1.33	0.46
S3	0.21	1.27	0.39
	0.41	0.88	1.26
	0.63	0.90	2.24

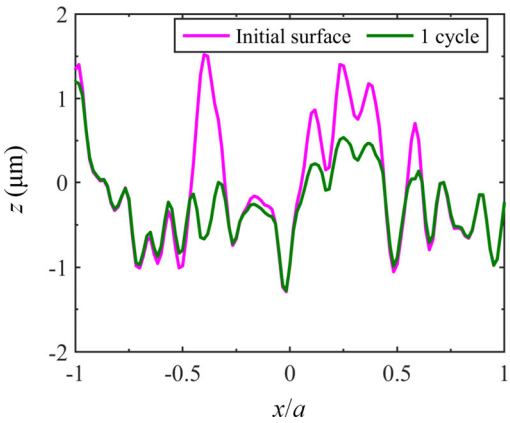

Fig. 13 Changes of surface topography at initial contact.

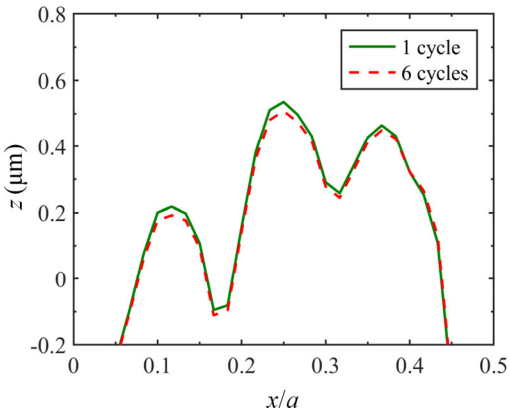

Fig. 14 Topographical changes of different cycles.

Table 4 displays the roughness *S*q of samples of different rough surfaces in the contact region of two-hertz contact half-width *a* under several contact cycles. The maximum roughness of the present model decreases to the surface roughness *S*q of sample S1 from 0.72 to 0.59 μm during the first cycle, and the roughness *S*q of subsequent cycle decreases linearly with the number of contact cycles, but the reduction amplitude is very small. The surface roughness reduces from *S*q = 0.72 to 0.58 μm after 6 contact cycles. After the first cycle, the surface roughness *S*q of different samples with small *S*q changes slightly. In the subsequent contact cycles, the roughness *S*q can be regarded as relatively constant. Thus, this paper only calculates the variation of roughness *S*q of three different surfaces of S1. The roughness reduction of the present model under the first cycle is greater than that of the Ren model. The plastic deformation degree of the surface after multiple cycles is evaluated by the change of roughness *S*q, and the plastic deformation of the roughness surface under the first cycle of the present model accounts for 66.7%–92.9% of the total plastic deformation of the six contact cycles. In the Ren model, the plastic deformation of the first cycle accounts for 50%–83.3% of the total plastic deformation of the six contact cycles, and the ratio is positively associated with the roughness *S*q. It is evident that the plastic deformation of multiple asperities under lubrication has limited influence on the overall surface topography, as the surface bearing capacity is improved after the plastic hardening caused by the initial contact deformation. Consequently, the research on the evolution of the contact surface topography should be given additional thought concerning surface wear and fatigue failure.

Table 4 Roughness *S*q (μm) during contact cycle.

Initial	1 cycle		6 cycles	
	Present	Ren	Present	Ren
0.22	0.20	0.21	0.19	0.20
0.47	0.40	0.42	0.39	0.41
0.72	0.59	0.62	0.58	0.60
0.20	0.19	0.19	—	—
0.42	0.39	0.41	—	—
0.68	0.62	0.65	—	—
0.21	0.20	0.20	—	—
0.41	0.36	0.38	—	—
0.63	0.55	0.57	—	—

4.3 Roughness and lubrication state of new model

The lubricating oil film prevents direct contact between the two solid surfaces. However, some surface asperities may directly contact when under load, altering the surface lubrication state. Additionally, the plastic deformation of the contact asperity may affect the surface lubrication state. As shown in Fig. 15, Figs. 15(a) and 15(b) respectively show the proportion of asperity contact area in total contact area and the proportion of plastic deformation area of contact surface in total contact area with different roughness *S*q. As illustrated in Fig. 15, the rough surfaces of different samples witnessed surface plastic deformation. The plastic deformation area of samples S1 and S3 increased and the increasing amplitude gradually decreased with the increase of *S*q. The solid contact area and surface plastic deformation area of S2 were considerably smaller

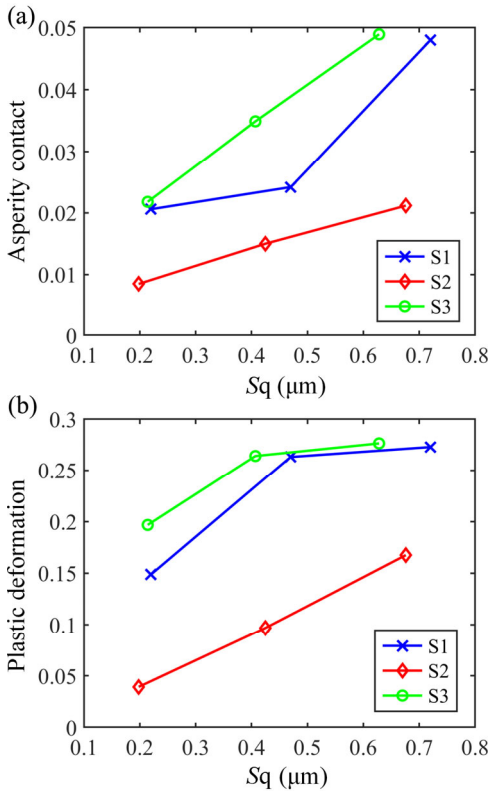

Fig. 15 Asperities contact and surface plastic deformation area of different roughness *S*q.

compared to the other two samples. Compared with the plastic deformation of the contact surface, the proportion of dry contact area of the local asperities of different samples is very small, less than 5%. Under the working conditions in this paper, the contact surface area is still mainly loaded by lubricating oil film. The compression and plastic deformation of surface asperities facilitate the separation of asperities on the rough surface, effectively enhancing the lubrication state of the contact surface.

5 Conclusions

In this paper, a new three-dimensional (3D) rough surface plastoelastohydrodynamic lubrication (R-PEHL) contact model is proposed by combining the elastic hydrodynamic lubrication contact numerical algorithm and the finite element method. Compared with the widely used Ren model for PEHL numerical calculation in R-PEHL research, the new model has higher calculation accuracy of contact stress and strain.The problem of rationality contradiction caused by smooth surface assumption of semi-infinite space in contact analysis is solved. Based on the new model, the contact analysis of different types of rough surface samples is carried out and compared with the calculation results of the Ren model. The study draws the following conclusions:

(1) The contact pressure of the new R-PEHL model is 200−800 MPa lower than that of the Ren model while the corresponding maximum Mises stress is 2.5%−26.6% greater. The oil film pressure fluctuation in the new model is gentler compared to the Ren model, and the high pressure of the Ren model is inclined to the oil outlet.

(2) The PEHL contact analysis of rough surface in the Ren model under the assumption of semi-infinite smooth surface cannot capture the plastic deformation of small asperities, and the position with large deformation and large deformation range is prone to the singularity of surface deformation surge. The relative error of contact deformation between the new model and the Ren model is 71%–173%, and the error decreases with the increase of *S*q.

(3) The new model demonstrates that the plastic deformation of the rough surfaces under lubrication condition mainly occurs in the first contact cycle. Furthermore, the plastic deformation of the first contact cycle accounts for 66.7%–92.9% of the total plastic deformation, while that of the Ren model accounts for 50%–83.3% of the total plastic deformation. Due to the plastic hardening of the material at the first contact, the plastic deformation of multiple asperities has little effect on overall surface topography.

(4) The new model reveals that the direct contact area of asperities on rough surfaces is relatively low, less than 5% of the nominal contact area. The plastic deformation of contact asperities reduces the dry contact area of asperities and enhances the lubrication state of rough surfaces.

The new model provides an innovative method and a fundamental model for the development and engineering application of fluid-structure coupling mechanics and interface lubrication mechanics.

Acknowledgements

The authors gratefully acknowledge the support of the National Key R&D Program of China (Grant No. 2022YFB3402902).

Declaration of competing interest

The authors have no competing interests to declare that are relevant to the content of this article.

References

[1] Reynolds O. IV. On the theory of lubrication and its application to Mr. Beauchamp tower's experiments, including an experimental determination of the viscosity of olive oil. *Phil Trans R Soc* **177**: 157–234 (1886)

[2] Dowson D, Higginson G R. A numerical solution to the elasto-hydrodynamic problem. *J Mech Eng Sci* **1**(1): 6–15 (1959)

[3] Ranger A P, Ettles C M M, Cameron A. The solution of the point contact elasto-hydrodynamic problem. *Proc R Soc Lond Ser A* **346**(1645): 227–244 (1975)

[4] Cheng H S. A refined solution to the thermal-elastohydrodynamic lubrication of rolling and sliding cylinders. *S L E Trans* **8**(4): 397–410 (1965)

[5] Zhu D, Wen S Z. A full numerical solution for the thermoelastohydrodynamic problem in elliptical contacts. *J Tribol* **106**(2): 246–254 (1984)

[6] Hsu C H, Lee R T. An efficient algorithm for thermal elastohydrodynamic lubrication under rolling/sliding line contacts. *J Tribol* **116**(4): 762–769 (1994)

[7] Ghosh M K, Pandey R K. Thermal elastohydrodynamic lubrication of heavily loaded line contacts—An efficient inlet zone analysis. *J Tribol* **120**(1): 119–125 (1998)

[8] Gu Z L, Zhu C C, Liu H J, Du X S. A comparative study of tribological performance of helical gear pair with various types of tooth surface finishing. *Ind Lubr Tribol* **71**(3): 474–485 (2019)

[9] Zhu D, Wang Q J. On the λ ratio range of mixed lubrication. *Proc Inst Mech Eng Part J J Eng Tribol* **226**(12): 1010–1022 (2012)

[10] Xu G, Sadeghi F. Thermal EHL analysis of circular contacts with measured surface roughness. *ASME J Tribol* **118**(3): 473–482 (1996)

[11] Hu Y Z, Zhu D. A full numerical solution to the mixed lubrication in point contacts. *J Tribol* **122**(1): 1–9 (2000)

[12] Ren N, Zhu D, Chen W W, Liu Y C, Wang Q J. A three-dimensional deterministic model for rough surface line-contact EHL problems. *J Tribol* **131**(1): 1 (2009)

[13] Zhu D, Liu Y C, Wang Q. On the numerical accuracy of rough surface EHL solution. *Tribol Trans* **57**(4): 570–580 (2014)

[14] Jacq C, Ne´lias D, Lormand G, Girodin D. Development of a three-dimensional semi-analytical elastic-plastic contact code. *J Tribol* **124**(4): 653–667 (2002)

[15] Polonsky I A, Keer L M. A numerical method for solving rough contact problems based on the multi-level multi-summation and conjugate gradient techniques. *Wear* **231**(2): 206–219 (1999)

[16] Liu S B, Wang Q. Studying contact stress fields caused by surface tractions with a discrete convolution and fast Fourier transform algorithm. *J Tribol* **124**(1): 36–45 (2002)

[17] Chiu Y P. On the stress field due to initial strains in a cuboid surrounded by an infinite elastic space. *J Appl Mech* **44**(4): 587 (1977)

[18] Chiu Y P. On the stress field and surface deformation in a half space with a cuboidal zone in which initial strains are uniform. *J Appl Mech* **45**(2): 302 (1978)

[19] Love A E H. *A Treatise on the Mathematical Theory of Elasticity*. New York (USA): Dover, 1944.

[20] Lemaitre J, Chaboche J L, Maji A K. *Mechanics of solid materials*. *J Eng Mech* **119**(3): 642–643 (1993)

[21] Ren N, Zhu D, Chen W W, Wang Q J. Plasto-elastohydrodynamic lubrication (PEHL) in point contacts. *J Tribol* **132**(3): 1 (2010)

[22] He T, Wang J X, Wang Z J, Zhu D. Simulation of plasto-elastohydrodynamic lubrication in line contacts of infinite and finite length. *J Tribol* **137**(4): 041505 (2015)

[23] He T, Zhu D, Wang J X. Simulation of plasto-elastohydrodynamic lubrication in a rolling contact. *J Tribol* **138**(3): 031503 (2016)

[24] Azam A, Dorgham A, Morina A, Neville A, Wilson M C T. A simple deterministic plastoelastohydrodynamic lubrication (PEHL) model in mixed lubrication. *Tribol Int* **131**: 520–529 (2019)

[25] Lohner T, Ziegltrum A, Stemplinger J P, Stahl K. Engineering software solution for thermal elastohydrodynamic lubrication using multiphysics software. *Adv Tribol* **2016**: 6507203 (2016)

[26] Zhou Y, Zhu C C, Liu H J, Song H L. Investigation of contact performance of case-hardened gears under plasto-elastohydrodynamic lubrication. *Tribol Lett* **67**(3): 92 (2019)

[27] Cao H, Khan Z, Meng Y G. Comparison of rolling contact fatigue life between elastohydrodynamic lubricated point contacts pre and post running-in treatment. *Tribol Int* **144**: 106089 (2020)

[28] Wang Q J, Zhu D. *Interfacial Mechanics: Theories and Methods for Contact and Lubrication*. Los Angeles (USA): CRC Press, 2019.

[29] Johnson K L. *Contact Mechanics*. Cambridge (UK): Cambridge University Press, 1985.

[30] Pei L, Hyun S, Molinari J, Robbins M. Finite element modeling of elasto-plastic contact between rough surfaces. *J Mech Phys Solids* **53**(11): 2385–2409 (2005)

[31] You S Y, Tang J Y, Zhou W, Zhou W H, Zhao J Y, Chen H F. Research on calculation of contact fatigue life of rough tooth surface considering residual stress. *Eng Fail Anal* **140**: 106459 (2022)

[32] Belytschko T, Liu W K, Moran B, Elkhodary K. *Nonlinear Finite Elements for Continua and Structures*. New York (USA): John Wiley & Sons Inc., 2000.

[33] Zugelj B B, Kalin M. Submicron-scale experimental analyses of multi-asperity contacts with different roughnesses. *Tribol Int* **119**: 667–671 (2018)

[34] Zhang F K, Liu J H, Ding X Y, Wang R L. Experimental and finite element analyses of contact behaviors between non-transparent rough surfaces. *J Mech Phys Solids* **126**: 87–100 (2019)

[35] Li L, Tang J Y, Wen Y Q, Zhu C C. Numerical simulation of ultrasonic-assisted grinding surfaces with fast Fourier transform. *J Tribol* **142**(9): 092301 (2020)

Shengyu YOU. He received his bachelor degree in mechanical engineering from Central South University, China, in 2017. Then, he is a Ph.D. student in the State Key Laboratory of Precision Manufacturing for Extreme Service Performance at the same university. His research areas cover tribology and contact fatigue and wear.

Jinyuan TANG. He received his M.S. degree in mechanical engineering from Central South University, China. He joined the State Key Laboratory of Precision Manufacturing for Extreme Service Performance at Central South University since 1988. His research areas cover intelligent manufacturing of high performance devices, and design theory of high performance power transmission device.

Qiang WANG. He received his Ph.D. degree in materials science and engineering from Harbin Institute of Technology, Harbin, China. He joined the State Key Laboratory of Precision Manufacturing for Extreme Service Performance at Central South University since 2021. His research areas cover anti-fatigue design and manufacturing of mechanical parts and components.